Supplementary Information

Amorphization and Defect Engineering in Constructing Ternary Composite Ag/$PW_{10}V_2$/am-TiO_{2-x} for Enhanced Photocatalytic Nitrogen Fixation

Caiting Feng,[a] Panfeng Wu,[b] Qinlong Li,[a] Jiquan Liu,*[a] Danjun Wang,[c] Bin Liu,[a] Tianyu Wang,[a] Huaiming Hu,[a] and Ganglin Xue*[a]

[a.] *Key Laboratory of Synthetic and Natural Functional Molecule Chemistry, College of Chemistry & Materials Science, Northwest University, Xi'an, 710127, P. R. China*

E-mail: jiquan-liu@nwu.edu.cn, xglin707@163.com

[b.] *School of Chemistry and Chemical Engineering, Xi'an Shiyou University, Xi'an, 710065, P. R. China*

[c.] *Shaanxi Key Laboratory of Chemical Reaction Engineering, College of Chemistry & Chemical Engineering, Yan'an University, Yan'an, 716000, P. R. China*

Table of contents

1. Experimental section

NH_3/NH_4^+ concentration determination and $^{15}N_2$ isotope labeling experiment

NH_3/NH_4^+ concentration was determined by the spectrophotometry method using Nessler's reagent as color developer.[1] First, clear reaction solution (2.5 mL) and deionized water (2.5 mL) was transferred to a 25 mL colorimetric tube, followed by adding potassium sodium tartrate solution (0.1 mL, 0.5 g mL^{-1}) and Nessler's reagent (0.1 mL). Then, the mixture was allowed to stand for 10 min at room temperature. Afterwards, the absorbance of the solution was recorded on SP-756P UV-visible spectrophotometer. The concentration of NH_3/NH_4^+ was calculated according to the absorbance at λ = 420 nm, where calibration curve (Fig. S8) was obtained using NH_4Cl standard solutions with concentration of 0.0, 1.0, 2.0, 3.0, 4.0, 5.0 mg L^{-1}.

Photocatalytic degradation of methyl orange (MO) under simulated sunlight

The photocatalytic activity of as-prepared catalysts was investigated through degradation of MO under simulated sunlight, using a 500 W xenon lamp as illuminant at a constant temperature (25°C). Typically, 40 mg catalyst was added into 30 mL MO aqueous solution (10 mg L^{-1}, pH = 2). Before irradiation, the mixture solution was continuously stirred in darkness for 30 min to achieve the equilibrium of adsorption-desorption between the photocatalyst and pollutant. During irradiation (without filter, 320 nm < λ < 800 nm), a certain amount of the suspension was withdrawn at 15 min interval. After centrifugation, the absorbance of supernatant at 507 nm was recorded.

2. Supplementary Scheme, Figures, Tables and Discussion

Table S1. Ti, W, and Ag weight fractions (in wt%) in $PW_{10}V_2$/am-TiO_{2-x}-*z* and Ag/$PW_{10}V_2$/am-TiO_{2-x}-*y* composites (*z*% is the theoretic $PW_{10}V_2$ fraction in wt%, *y*% is the theoretic Ag fraction in wt%)

Composites	Ti/wt% (theoretic value)	W/wt% (theoretic value)	Ag/wt% (theoretic value)
$PW_{10}V_2$/am-TiO_{2-x}-9.8	55.1(54.0)	6.5 (6.9)	–
$PW_{10}V_2$/am-TiO_{2-x}-14.5	52.0(51.2)	9.7(10.4)	–
$PW_{10}V_2$/am-TiO_{2-x}-19.5	48.5(48.1)	13.0(13.7)	–
Ag/$PW_{10}V_2$/am-TiO_{2-x}-0.5	50.8(50.9)	11.1(10.3)	0.6(0.5)
Ag/$PW_{10}V_2$/am-TiO_{2-x}-1.0	48.4(50.6)	11.2(10.3)	0.9(1.0)
Ag/$PW_{10}V_2$/am-TiO_{2-x}-1.5	47.6(50.4)	10.8(10.2)	1.4(1.5)
Ag/$PW_{10}V_2$/am-TiO_{2-x}-2.0	49.2(50.1)	10.1(10.2)	2.1(2.0)

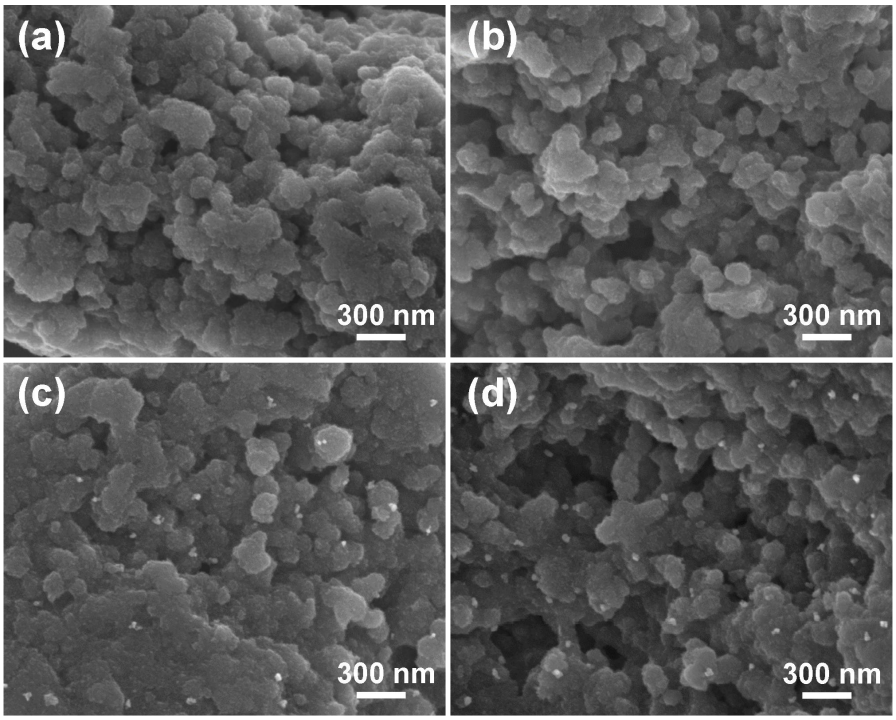

Fig. S1. SEM images of (a) am-TiO_{2-x}, (b) $PW_{10}V_2$/am-TiO_{2-x}, (c) Ag/am-TiO_{2-x} and (d) Ag/$PW_{10}V_2$/am-TiO_{2-x}

The morphologies of am-TiO_{2-x}, $PW_{10}V_2$/am-TiO_{2-x}, Ag/am-TiO_{2-x} and Ag/$PW_{10}V_2$/am-TiO_{2-x} are displayed in Fig. S1. All of them exhibit mainly a three-dimensional worm-like interconnected meso-structure packed by fine nanoscale particles (ca.120 nm) with uniform distribution.

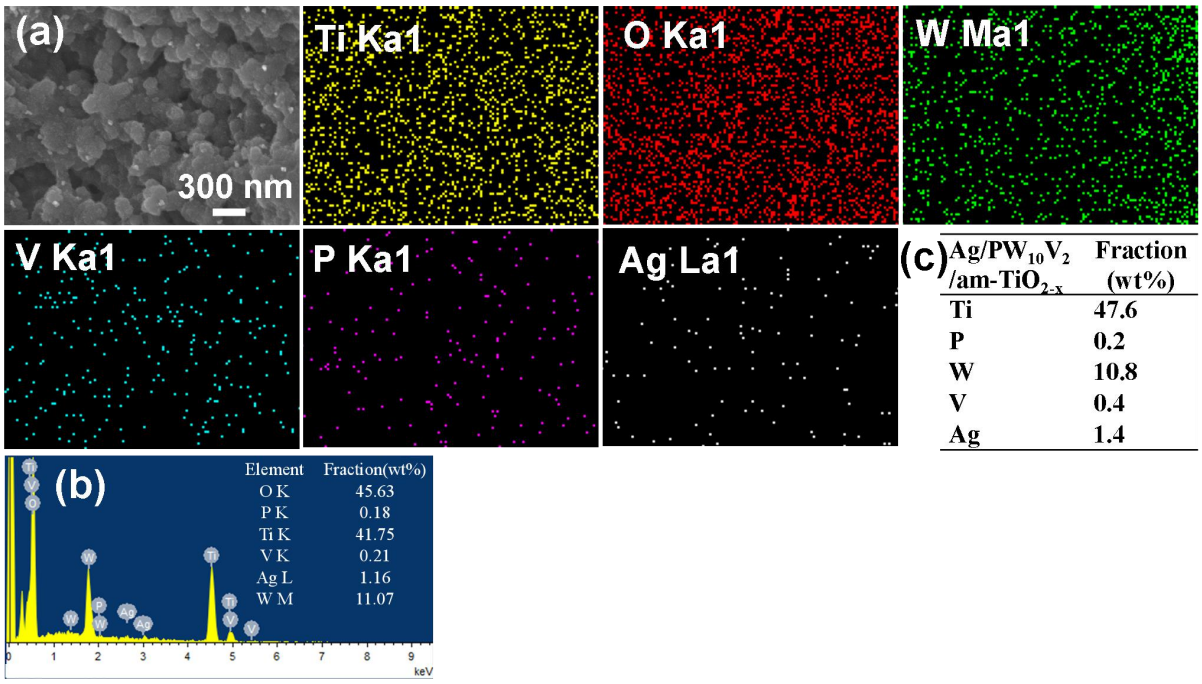

(c)

$Ag/PW_{10}V_2/am\text{-}TiO_{2-x}$	Fraction (wt%)
Ti	47.6
P	0.2
W	10.8
V	0.4
Ag	1.4

Fig. S2. (a) EDX-mapping, (b) EDX spectrum and (c) ICP-AES for $Ag/PW_{10}V_2/am\text{-}TiO_{2-x}$ composite

The successful synthesis of $Ag/PW_{10}V_2/am\text{-}TiO_{2-x}$ is confirmed by EDX, EDX-mapping, ICP-MS experiments, where elements Ti, P, W, V, O and Ag co-exist in the ternary composite (Fig. S2). Both EDX and ICP-AES outcomes agree with each other very well, demonstrate the loadings of $PW_{10}V_2$ and Ag NPs on $am\text{-}TiO_{2-x}$ fit the theoretic values (Table S1).

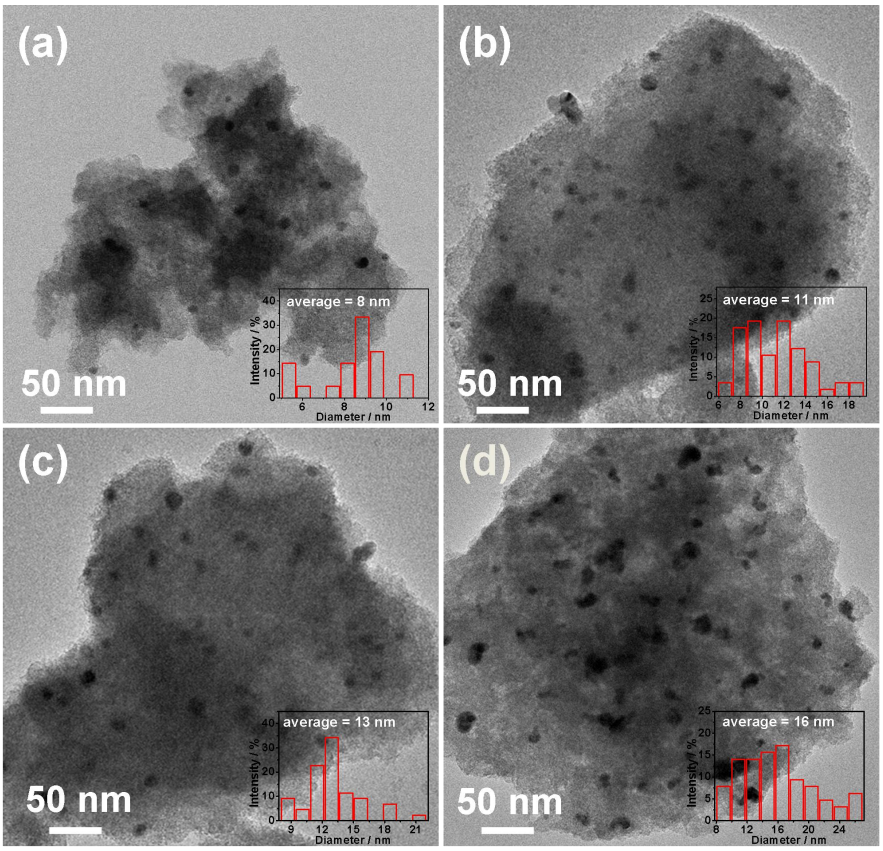

Fig. S3. TEM images of the as-synthesized ternary composites Ag/$PW_{10}V_2$/am-TiO_{2-x}-*y* (a) *y* = 0.5, (b) *y* = 1.0, (c) *y* = 1.5 and (d) *y* = 2.0 (*y*% is the theoretic Ag fraction in wt%)

TEM images of Ag/$PW_{10}V_2$/am-TiO_{2-x}-*y* (*y* = 0.5, 1.0, 1.5, 2.0) are displayed in Fig. S3, together with the size distribution of Ag NPs (inserts). The average particle size of Ag NPs increases with the Ag loading, and aggregation of Ag NPs becomes severe when the loading increases to 2.0%.

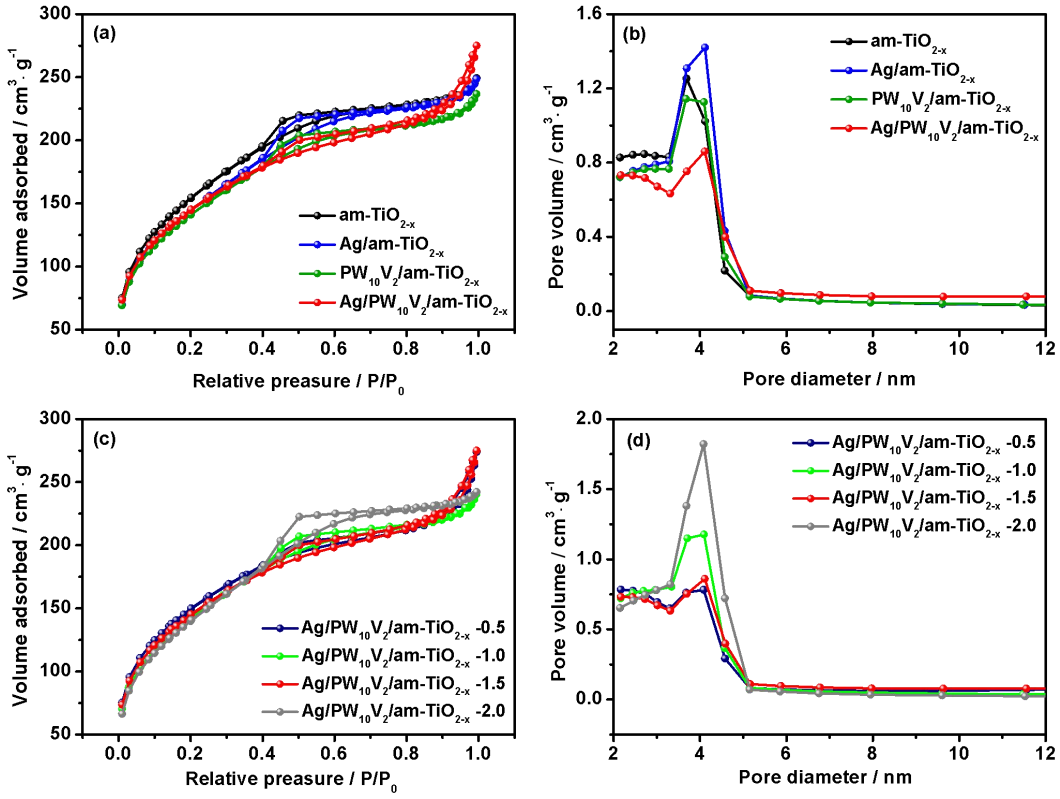

Fig. S4. N_2-absorption-desorption isotherms and BJH pore size distribution curves for (a, b) am-TiO_{2-x}, $PW_{10}V_2$/am-TiO_{2-x}, Ag/am-TiO_{2-x} and Ag/$PW_{10}V_2$/am-TiO_{2-x}, as well as (c, d) Ag/$PW_{10}V_2$/am-TiO_{2-x} composites with different Ag loadings

Table S2. Textural parameters of as-synthesized catalysts

Samples	BET surface area (m^2 g^{-1})	Pore size (nm)	Pore volume (cm^3 g^{-1})
am-TiO_{2-x}	555.29	3.68	0.37
Ag/am-TiO_{2-x}	524.32	4.08	0.39
$PW_{10}V_2$/am-TiO_{2-x}	508.13	3.85	0.35
Ag/$PW_{10}V_2$/am-TiO_{2-x}-1.5	513.38	4.11	0.38
Ag/$PW_{10}V_2$/am-TiO_{2-x}-0.5	528.88	4.08	0.37
Ag/$PW_{10}V_2$/am-TiO_{2-x}-1.0	512.87	4.08	0.35
Ag/$PW_{10}V_2$/am-TiO_{2-x}-2.0	512.52	4.06	0.36

The texture of heterogeneous catalyst greatly affects its catalytic performance with respect to the number of active sites and the accessibility of active sites to the substrate. Herein, nitrogen adsorption-desorption isotherms are shown in Figs. S4a and 4b for am-TiO_{2-x}, Ag/am-TiO_{2-x}, $PW_{10}V_2$/am-TiO_{2-x} and Ag/$PW_{10}V_2$/am-TiO_{2-x}. Type IV isotherms together with type H2 hysteresis loops indicate the presence of mesopores, whose average diameters are determined to be 3-5 nm according to by BJH pore size distribution curves (Fig. S4b). As listed in Table S2, the BET surface areas of am-TiO_{2-x}, Ag/am-TiO_{2-x}, $PW_{10}V_2$/am-TiO_{2-x} and Ag/$PW_{10}V_2$/am-TiO_{2-x} are measured to be 555, 508, 524 and 513 $m^2\ g^{-1}$, respectively. Such high specific surface area is beneficial to the adsorption of nitrogen molecules, and their mesoporous feature facilitates mass transfer in the heterogeneous catalytic process. The presence of Ag NPs and $PW_{10}V_2$ on the inner surface of am-TiO_{2-x} may results in reduced BET surface area for $PW_{10}V_2$ and/or Ag NPs doped composites. In the ternary composites, the texture features do not vary significant, when different amounts of Ag NPs are loaded. This might hint that suitable decorating fraction would not cause the blockage or collapse of am-TiO_{2-x} matrix. Of course, high loading of Ag leads to the aggregation of Ag NPs as revealed by TEM (Fig. S3).

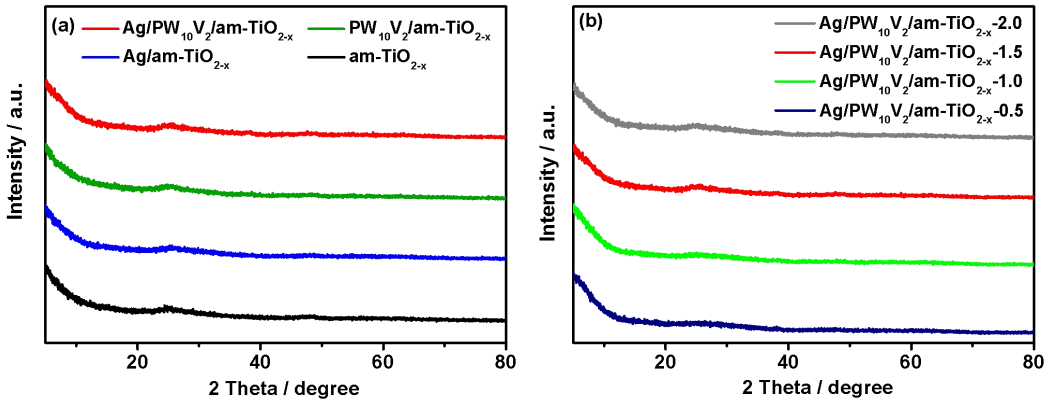

Fig. S5. PXRD of (a) am-TiO_{2-x}, $PW_{10}V_2$/am-TiO_{2-x}, Ag/am-TiO_{2-x} and Ag/$PW_{10}V_2$/am-TiO_{2-x}, as well as (b) Ag/$PW_{10}V_2$/am-TiO_{2-x} composites with different Ag loadings

Fig. S5a shows the PXRD patterns for am-TiO_{2-x}, $PW_{10}V_2$/am-TiO_{2-x}, Ag/am-TiO_{2-x} and Ag/$PW_{10}V_2$/am-TiO_{2-x}. The amorphous nature of am-TiO_{2-x} is confirmed due to the absence of characteristic diffractions for rutile or anatase phase. It might relate to abundant OVs in its matrix, which is thought to be favorable for adsorption and activation of substrates in the photo-driven process.[2] Then, the high dispersion of polyoxometalate is confirmed owing to the fact that no diffractions present in the composites. Similarly, fine dispersion of Ag NPs over Ag/$PW_{10}V_2$/am-TiO_{2-x} composites with different Ag loadings is obtained (Fig. S5b), which is in well agreement with TEM observations (Fig. 1 and Fig. S3).

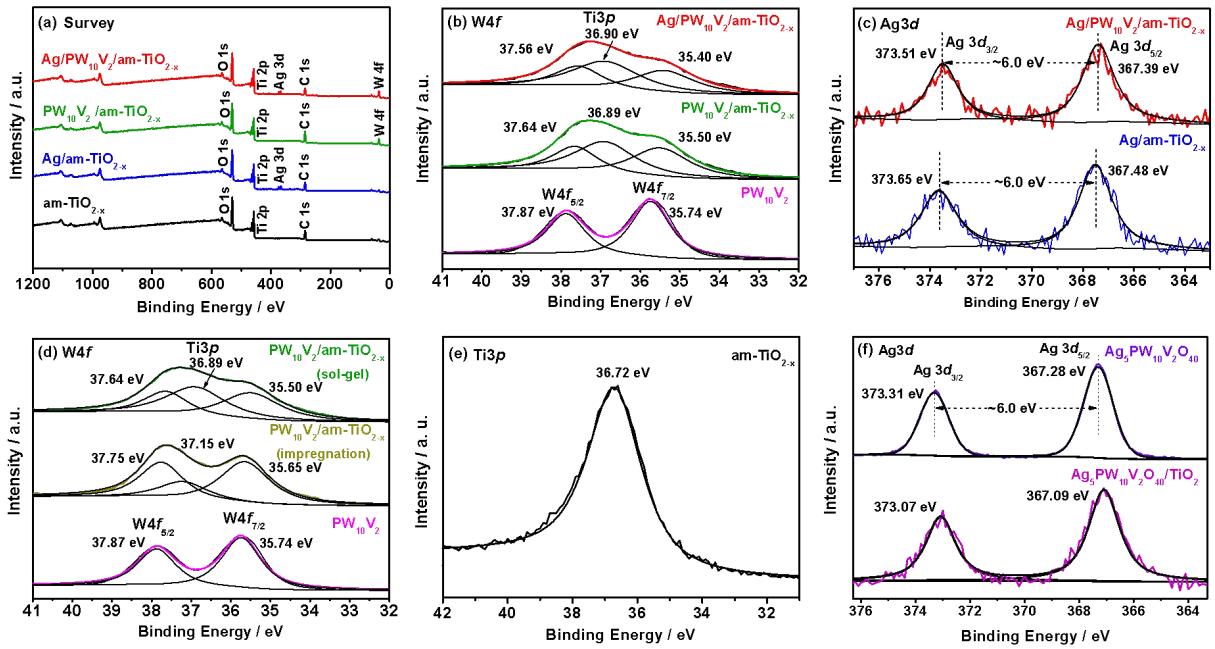

Fig. S6. (a) XPS survey spectra of different catalysts, and high-resolution spectra for (b, d) W4*f*, (c, f) Ag3*d* and (e) Ti3*p*

In the XPS survey spectrum of Ag/$PW_{10}V_2$/am-TiO_{2-x} (Fig. S6a), Ag, W, Ti and O co-exist in the composite, and similar observations are found over binary composites (Ag/am-TiO_{2-x} and $PW_{10}V_2$/am-TiO_{2-x}). The high-resolution spectra for W4*f* are displayed in Figs. S6b and S6d. The broad line can be deconvoluted into two sub-peaks, the binding energy of ca.37.8 and 35.7 eV are ascribed to W4$f_{5/2}$ and W4$f_{7/2}$ for $PW_{10}V_2$, respectively. After immobilizing $PW_{10}V_2$ on am-TiO_{2-x}, puny negative shifts are observed for W4*f* signals. This is an indication of strong interaction between $PW_{10}V_2$ and am-TiO_{2-x}. It agrees well with the positive shift of Ti2*p* signals (Fig. 3a in main text). With respect to the composites, three sub-peaks are obtained after deconvolution, and the emerged peak at ca. 36.9 eV is attributed to the Ti3*p*. This is further confirmed by control experiment, where binding energy of 36.72 eV is observed in the case of am-TiO_{2-x} (Fig. S6e). Moreover, the binding energies of 373.6 and 367.4 eV are ascribed to Ag3$d_{3/2}$ and Ag3$d_{5/2}$, respectively, for composites with Ag NPs decoration (Fig. S6c).

Here, ca. 6.0 eV interval between Ag3$d_{3/2}$ and Ag3$d_{5/2}$ peaks is an indication of metallic feature of Ag NPs.

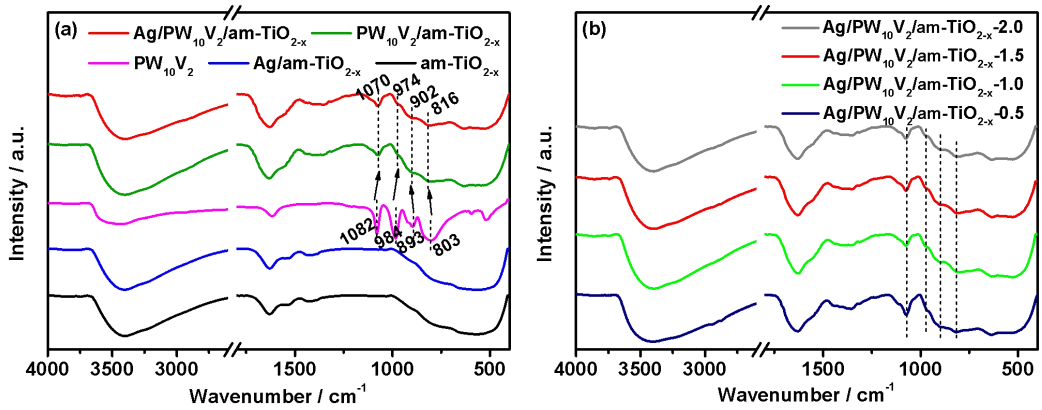

Fig. S7. FT-IR spectra of (a) am-TiO_{2-x}, $PW_{10}V_2$/am-TiO_{2-x}, Ag/am-TiO_{2-x} and Ag/$PW_{10}V_2$/am-TiO_{2-x}, as well as (b) Ag/$PW_{10}V_2$/am-TiO_{2-x} catalysts with different Ag loadings

Structural integrity of the Keggin unit in the Ag/$PW_{10}V_2$/am-TiO_{2-x} composite is confirmed by FT-IR (Fig. S7). For $PW_{10}V_2$ (Fig. S7a), the vibration modes relating to the Keggin unit emerge at 1082 (P-O_a), 984 cm^{-1} (W=O_d), 893 (W-O_c-W), and 803 cm^{-1} (W-O_b-W).[3] After forming $PW_{10}V_2$/am-TiO_{2-x} and Ag/$PW_{10}V_2$/am-TiO_{2-x} composites, the corresponding vibration frequencies shift to 1070, 974, 902 and 816 cm^{-1}, respectively. The result implies that the primary Keggin structure stays intact when introducing to am-TiO_{2-x} framework by current synthetic route. Compared to parent $PW_{10}V_2$, these shifts of frequencies are due to strong interactions between the Keggin unit and am-TiO_{2-x}. According to the previous report,[4] Keggin units are supposed to be anchored on TiO_2 via W-O-Ti covalent bonds, hydrogen bonds and acid-base interactions between Keggin anion and ≡Ti-OH groups on the surface of TiO_2. This guarantees the intactness of Ag/$PW_{10}V_2$/am-TiO_{2-x} against the liberation of $PW_{10}V_2$ from am-TiO_{2-x} matrix during the preparation process and subsequent catalytic experiments.

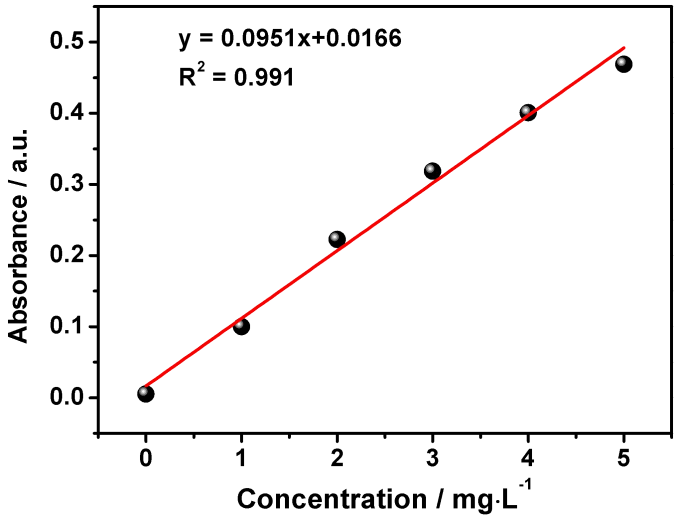

Fig. S8. Calibration curve for NH_4Cl standard solution using Nessler's reagent as color developer in spectrophotometry

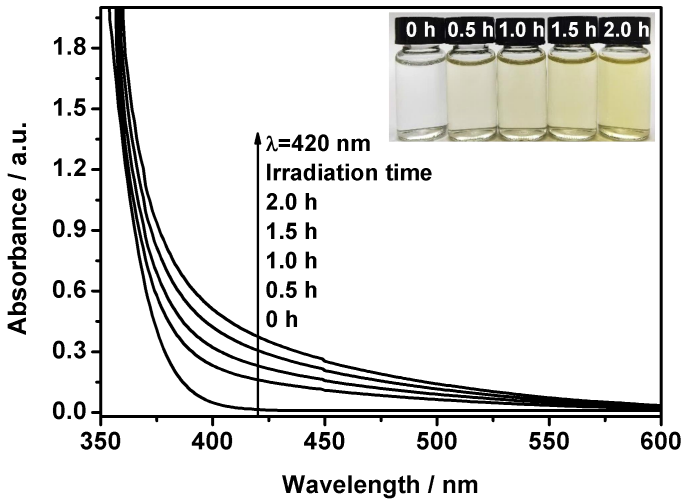

Fig. S9. Absorbance of reaction medium using Nessler's reagent as color developer to determine NH_3/NH_4^+ in spectrophotometry

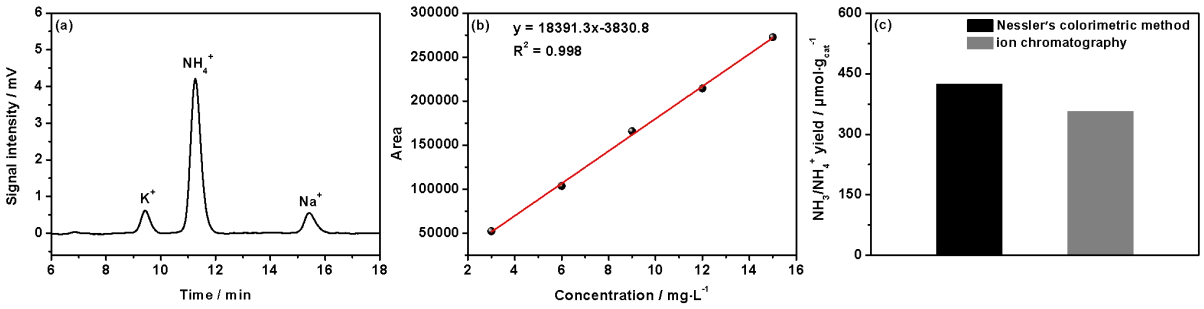

Fig. S10. (a) Ion-chromatography for generated NH_3/NH_4^+ over $Ag/PW_{10}V_2/am\text{-}TiO_{2\text{-}x}$ using N_2 and water as feedstocks, (b) Calibration curve for NH_4Cl standard solution using ion-chromatography and (c) The comparison of NH_3/NH_4^+ productions over $Ag/PW_{10}V_2/am\text{-}TiO_{2\text{-}x}$ determined by ion chromatography and Nessler's colorimetric method

Photo-driven nitrogen reduction is carried out under N_2 atmosphere, and the concentration of generated NH_3/NH_4^+ is measured by ion chromatography. As shown in Fig. S10a, the retention time for NH_4^+ locates at 11.3 min. The NH_4^+ yield is determined to be 356.7 μmol g_{cat}^{-1}, which is consistent with the experimental results obtained by the Nessler's colorimetric method (Fig. S10c).

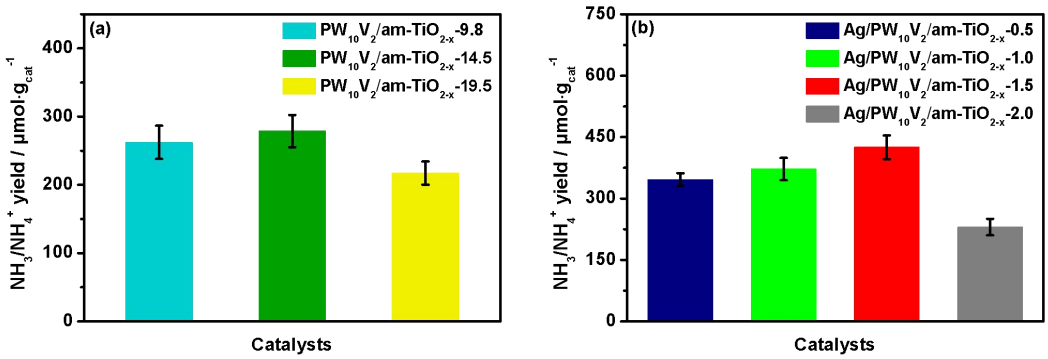

Fig. S11. NH_3/NH_4^+ productions under simulated sunlight irradiation in nitrogen atmosphere over (a) $PW_{10}V_2$/am-TiO_{2-x}-*z* and (b) Ag/$PW_{10}V_2$/am-TiO_{2-x}-*y*, respectively. (*z*% is the theoretic $PW_{10}V_2$ fraction in wt%, *y*% is the theoretic Ag fraction in wt%)

The loading effects of $PW_{10}V_2$ and Ag NPs are investigated. The $PW_{10}V_2$ loading is optimized to be 14.5wt% in $PW_{10}V_2$/am-TiO_{2-x} composites. Then, 1.5wt% of Ag NPs in Ag/$PW_{10}V_2$/am-TiO_{2-x} is beneficial to photo-driven nitrogen reduction reaction (Fig. S11). It is plausible that less catalytic sites are available for nitrogen activation when excess $PW_{10}V_2$ units or Ag NPs are introduced to am-TiO_{2-x}.

Table S3. The reported results for photo-driven nitrogen reduction reaction using water and pure nitrogen as feedstocks without introducing scavenger

Catalysts	Scavenger	Light source	NH_3/NH_4^+production rate / μmol g_{cat}^{-1} h^{-1}	Ref.
CuCr-LDH	No	visible light	57.2[a]	5
MoS_2	No	500 W Xe lamp	325 (pH=3.5)	6
HWO/C500	No	simulated sunlight	205	7
Bi_5O_7Br-40	No	visible light	1272[b]	8
Bi_5O_7Br-NT	No	visible light	1380	9
Fe-3D graphene	No	500 W Hg lamp	22.7[c]	10
SiW_{12}/K-C_3N_4	No	Xe lamp (100 mW cm^{-2})	70.6[d]	11
Mo-doped $W_{18}O_{49}$	Na_2SO_3 aqueous solution,1 mM	300 W Xe lamp	195.5	12
Bi_2MoO_6/OV-BiOBr	No	300 W Xe lamp	90.7	13
$Bi_4O_5Br_2$/ZIF-8	No	simulated sunlight	16.4[e]	14
AgCl/δ-Bi_2O_3	No	visible light	606	15
TiO_2 nanotubes	methanol	simulated sunlight	106.6	16
MoO_{3-x}	No	300 W Xe lamp	1.11[f]	17
H-Bi_2MoO_6	No	simulated sunlight	1300	18
BiOBr-001-OV	No	visible light	104.2	19
Ni_2P/$Cd_{0.5}Zn_{0.5}S$	No	visible light	253.7[g]	20
Ag-δ-Bi_2O_3	No	visible light	1.7[h]	21
am-TiO_{2-x}	No	**simulate sunlight**	**142.2**	**Present work**
Ag/$PW_{10}V_2$/am-TiO_{2-x}	No	**simulate sunlight**	**251.2**	**Present work**

[a]NH_3/NH_4^+ production is 142.9 μmol L^{-1}, reaction conditions: 50mg catalyst, 20 mL deionized water, 1h.

[b]NH_3/NH_4^+ production rate is 12.72 mM g_{cat}^{-1} h^{-1} in 100 mL reaction medium.

[c]NH_3/NH_4^+ production rate is 408 μg g_{cat}^{-1} h^{-1}.

[d]NH_3/NH_4^+ production rate is 353.2 μM g_{cat}^{-1} h^{-1} in 200 mL reaction medium.

[e]NH_3/NH_4^+ production rate is 327.338 μmol L^{-1} h^{-1} g_{cat}^{-1} in 50 mL reaction medium.

[f]NH_3/NH_4^+ production rate is 11.1 μmol L^{-1} g_{cat}^{-1} h^{-1} in 100 mL reaction medium.

[g]NH_3/NH_4^+ production is 101.5 μmol L^{-1} h^{-1}, reaction conditions: 0.02 g catalyst, 50 mL deionized water.

[h]NH_3/NH_4^+ production is 5.1 μmol L^{-1}, reaction conditions: 0.2 g catalyst, 200 mL deionized water, 3h.

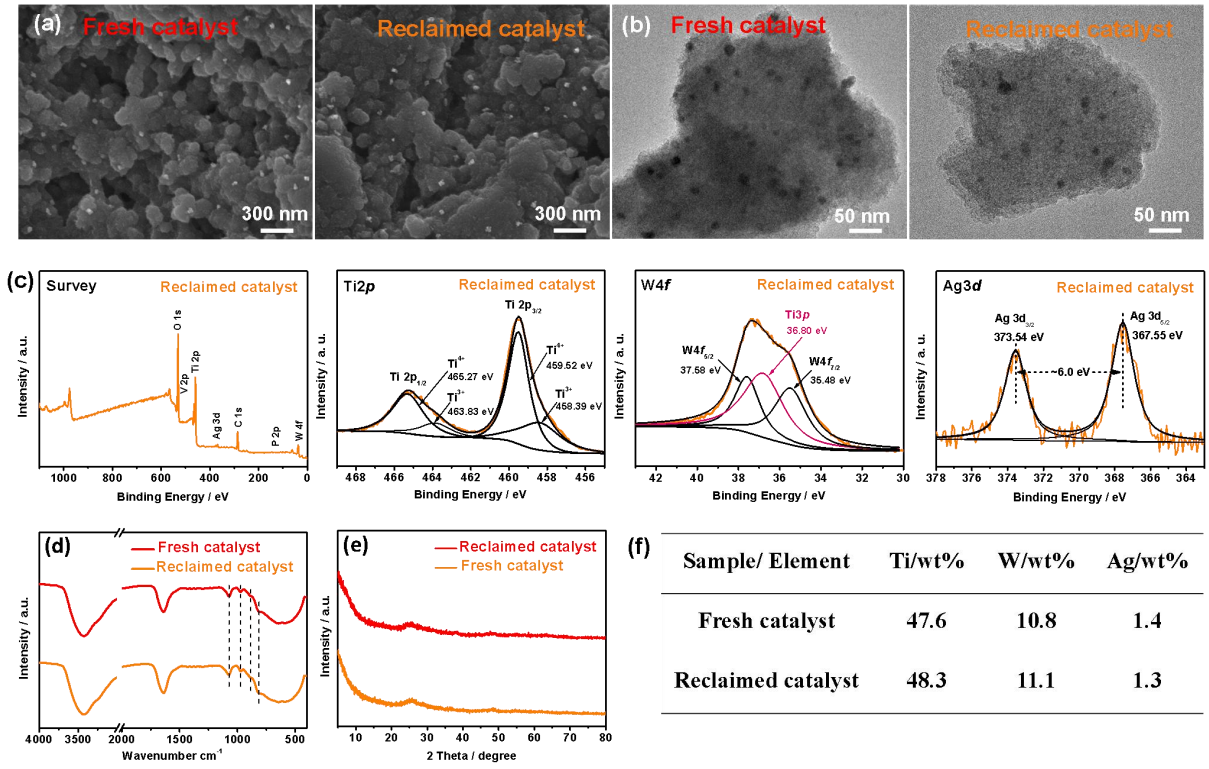

(f)

Sample/ Element	Ti/wt%	W/wt%	Ag/wt%
Fresh catalyst	47.6	10.8	1.4
Reclaimed catalyst	48.3	11.1	1.3

Fig. S12. (a) SEM images, (b) TEM images, (c) XPS spectra, (d) FT-IR spectra, (e) PXRD patterns as well as (f) Ti, W and Ag fractions of Ag/$PW_{10}V_2$/am-TiO_{2-x} before and after photo-driven nitrogen reduction reaction under simulated sunlight irradiation

The stability and recyclability of Ag/$PW_{10}V_2$/am-TiO_{2-x} are tested (Fig. 2f in main text). Under simulated sunlight irradiation, negligible activity loss is obtained over Ag/$PW_{10}V_2$/am-TiO_{2-x} after eight cycles in pure nitrogen atmosphere. The texture property and chemical information of the reclaimed catalyst are reflected by SEM, TEM, XPS, FT-IR and XRD (Figs. S12a-e). All these outcomes indicate the intactness of Ag/$PW_{10}V_2$/am-TiO_{2-x} during photo-driven catalytic process. Its excellent stability and recyclability are attributed to the strong interactions between $PW_{10}V_2$ and am-TiO_{2-x}, as well between Ag and am-TiO_{2-x}. This significantly inhibits the liberation of $PW_{10}V_2$ and Ag from the composite during the catalytic process, as confirmed by ICP-AES (Fig. S12f).

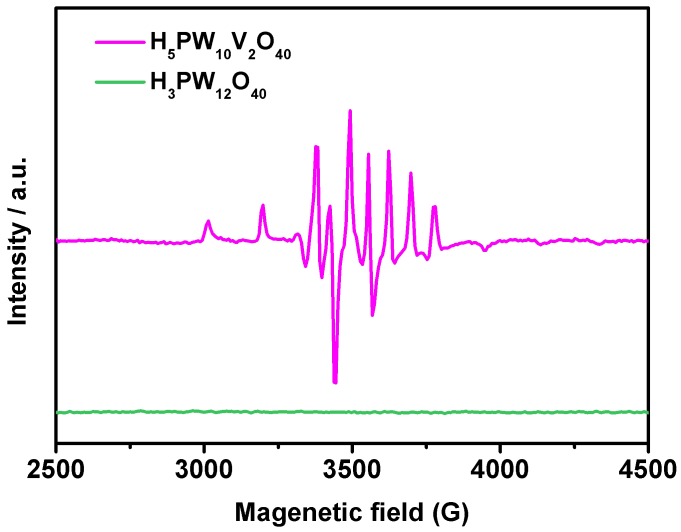

Fig. S13. EPR spectra of $PW_{10}V_2$ and PW_{12}

As shown in Fig. S13, compared to $H_3PW_{12}O_{40}$ (PW_{12}), EPR signal of $PW_{10}V_2$ is originated from paramagnetic $O=V^{2+}$ centers of $H_5V^{V}O_4V^{IV}W_{11}O_{36}$, which is a typical impurity in synthesized $PW_{10}V_2$.[22] For composites, EPR signal for OVs is clearly present in the spectra, whilst these resonances for $O=V^{2+}$ are less visible, mainly due to relative low faction of $O=V^{2+}$ species. In EPR test, the loadings of parent $PW_{10}V_2$ and $PW_{10}V_2$-based composites are kept in the same volume. The density of $PW_{10}V_2$ is around four times of $PW_{10}V_2$-based composites. The ratio of EPR signal intensity for $O=V^{2+}$ species in parent $PW_{10}V_2$ is approximately twice (in volume) but half (in weight) of that for OVs in $PW_{10}V_2$-based composites. When consideration the fraction of $PW_{10}V_2$ (14.5 wt%) in the composites, the signal intensity of $O=V^{2+}$ species is one fifteenth of that for OVs. Another possibility is that $H_5V^{V}O_4V^{IV}W_{11}O_{36}$ is not well fixed in the am-TiO_{2-x} matrix, nevertheless, deep mechanism of absence $O=V^{2+}$ signals in the composites will be well illustrated in the future investigations.

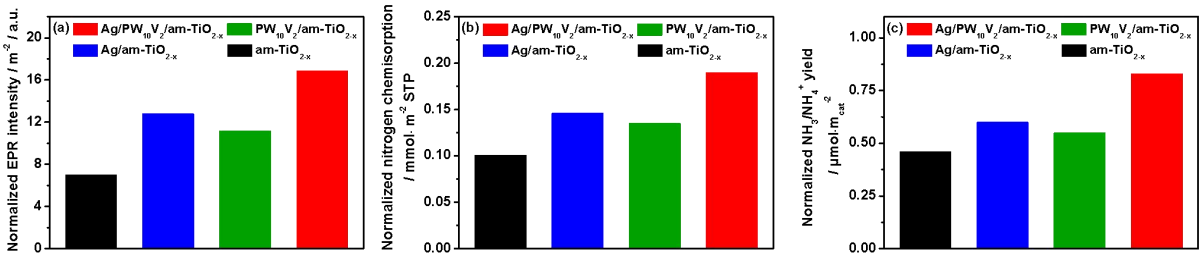

Fig. S14. Normalized (a) EPR intensity, (b) N_2 chemisorption amount and (c) NH_3/NH_4^+ productions for am-TiO_{2-x} based catalysts

To well illustrate the structure-reactivity relationship, EPR intensity, nitrogen chemisorption amount and NH_3/NH_4^+ productions are normalized by BET surface area (Fig. S14). It is obvious that the normalized EPR intensity, nitrogen chemisorption amount increases with the order of am-TiO_{2-x}, $PW_{10}V_2$/am-TiO_{2-x}, Ag/am-TiO_{2-x} and Ag/$PW_{10}V_2$/am-TiO_{2-x}, together with corresponding catalytic efficiency. This phenomenon strongly demonstrates that OVs play an important role in nitrogen adsorption and activation process.

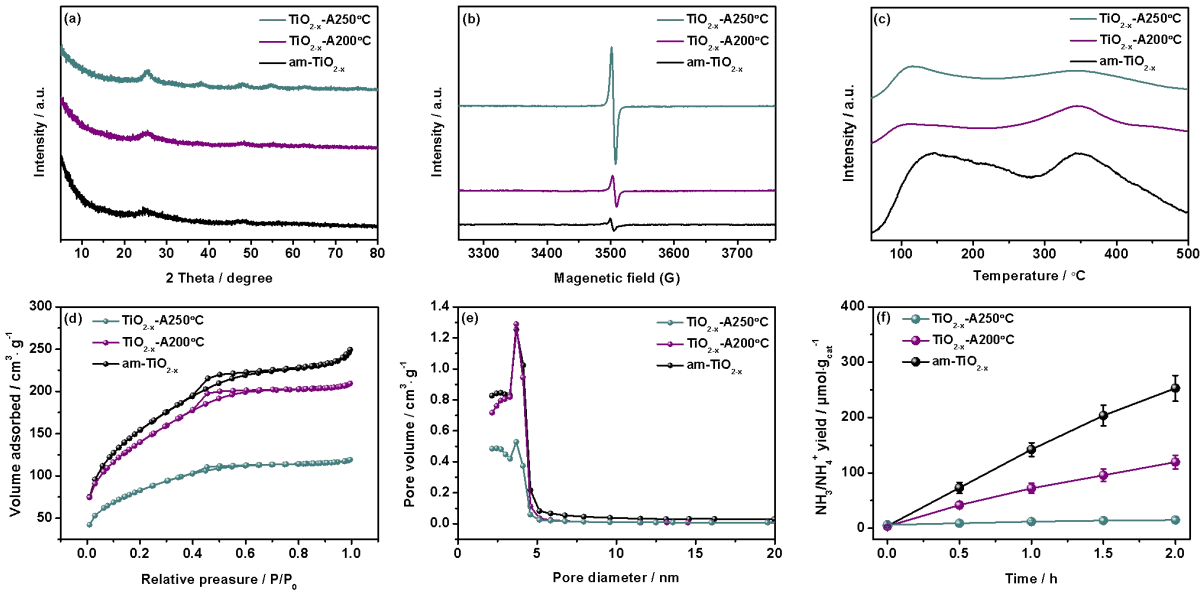

(g)

Catalyst	BET Surface Area ($m^2 \cdot g^{-1}$)	Pore Size (nm)	Pore Volume ($cm^3 \cdot g^{-1}$)	Intensity of EPR	Quantity of chemical adsorption for N_2 ($mmol \cdot g^{-1}$)
am-TiO_{2-x}	555.29	2.67	0.37	0.6	56.3
TiO_{2-x}-A200°C	503.41	2.54	0.32	1.6	17.8
TiO_{2-x}-A250°C	285.90	2.45	0.18	6.0	6.2

Fig. S15. (a) PXRD patterns, (b) EPR spectra, (c) N_2-TPD profiles, (d) N_2-absorption-desorption isotherms, (e) BJH pore size distributions and (f) NH_3/NH_4^+ productions over am-TiO_{2-x}, TiO_{2-x}-A200°C and TiO_{2-x}-A250°C, as well as (g) the summary of concerned parameters

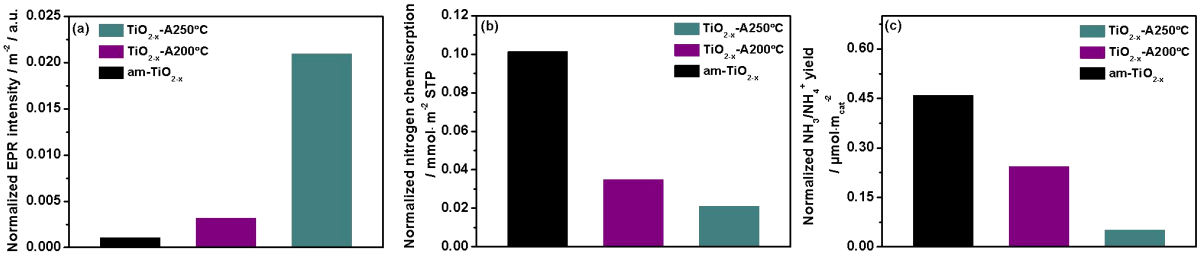

Fig. S16. Normalized (a) EPR intensity, (b) N_2 chemisorption amount and (c) NH_3/NH_4^+ productions for am-TiO_{2-x}, TiO_{2-x}-A200°C and TiO_{2-x}-A250°C

To elucidate the function of OVs, as-prepared am-TiO_{2-x} is calcinated at 200 and 250°C in air for 2 h, and denoted as TiO_{2-x}-A200°C and TiO_{2-x}-A250°C, respectively. As shown in Fig. S15, the EPR signal

of TiO_{2-x} intensified with increased calcination temperature, as well the slight improved crystallinity. For calcinated TiO_{2-x} at higher temperature (200°C or 250°C), the increased OVs are originated from lattice reformation of TiO_{2-x} when crystallizing from amorphous phase, in line with reported literature.[23] In the same time, nitrogen chemisorption amount, BET surface area and the NH_3/NH_4^+ production of TiO_{2-x} decrease along with raised calcination temperature. NH_3/NH_4^+ is almost undetectable over TiO_{2-x}-A250°C, although it exhibits strong EPR signal intensity. The nitrogen chemisorption amount can be well correlated to activity test. As shown in Fig. S16, it is obvious that the normalized nitrogen chemisorption amount decreases after calcination treatment, together with corresponding catalytic efficiency. This phenomenon strongly demonstrates that surface OVs involve in nitrogen adsorption and activation process, rather than the bulk OVs.

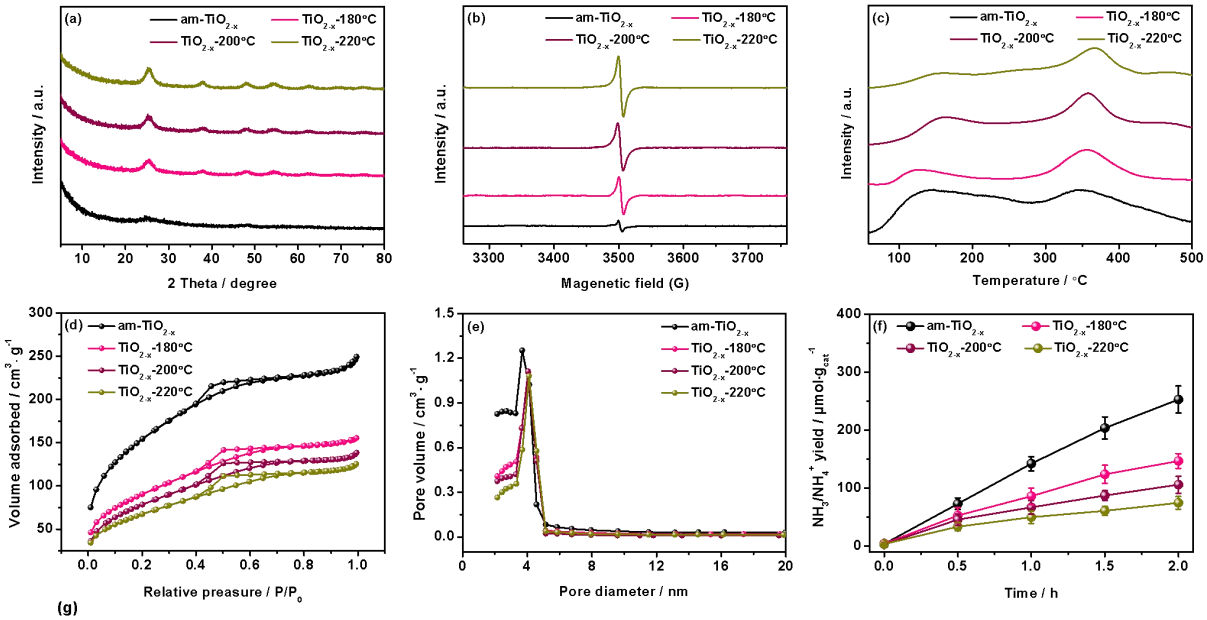

(g)

Catalyst	BET Surface Area ($m^2 \cdot g^{-1}$)	Pore Size (nm)	Pore Volume ($cm^3 \cdot g^{-1}$)	Intensity of EPR	Quantity of chemical adsorption for N_2 ($mmol \cdot g^{-1}$)
am-TiO_{2-x}	555.29	2.67	0.37	0.6	56.3
TiO_{2-x}-180°C	328.17	2.87	0.24	2.1	38.4
TiO_{2-x}-200°C	287.53	2.85	0.21	2.8	31.7
TiO_{2-x}-220°C	245.21	3.05	0.19	3.5	27.6

Fig. S17. (a) XRD patterns, (b) EPR spectra, (c) N_2-TPD profiles, (d) N_2-absorption-desorption isotherms, (e) BJH pore size distributions, (f) NH_3/NH_4^+ productions for am-TiO_{2-x}, TiO_{2-x}-180°C, TiO_{2-x}-200°C and TiO_{2-x}-220°C, as well as (g) the summary of concerned parameters

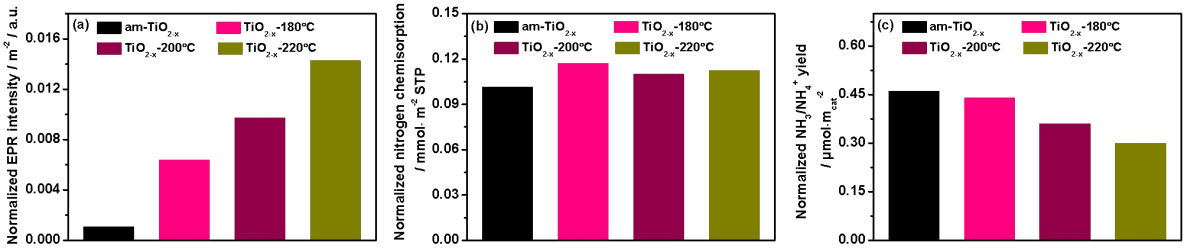

Fig. S18. Normalized (a) EPR intensity, (b) N_2 chemisorption amount and (c) NH_3/NH_4^+ productions for am-TiO_{2-x}, TiO_{2-x}-180°C, TiO_{2-x}-200°C and TiO_{2-x}-220°C

TiO_{2-x} with crystallinity are prepared in the same way by increasing the temperature of solvothermal synthesis from 180°C to 220°C, and denoted as TiO_{2-x}-180°C, TiO_{2-x}-200°C and TiO_{2-x}-220°C,

respectively. As shown in Fig. S17, the crystallinity of TiO_{2-x} becomes higher when raising the solvothermal temperature, as well the strengthened EPR signals for OVs. In the same way, the increased OVs are originated from certain changes on lattice during crystallization process.[23] However, this leads to reduced nitrogen chemisorption, BET surface area, and catalytic performance. As shown in Fig. S18, the normalized EPR signal intensity increases with the solvothermal temperature, while the normalized nitrogen chemisorption amount stays almost constant. This means that the density of bulk OVs increase yet surface OVs at each square meter does not alter. Of course, large surface area is beneficial to nitrogen chemisorption. Then, the normalized NH_3/NH_4^+ production over anatase TiO_{2-x} reduces, while the crystallinity of TiO_{2-x} enhances along with the solvothermal temperature. This outcome highlights the importance of amorphous structure in photo-driven catalytic process.

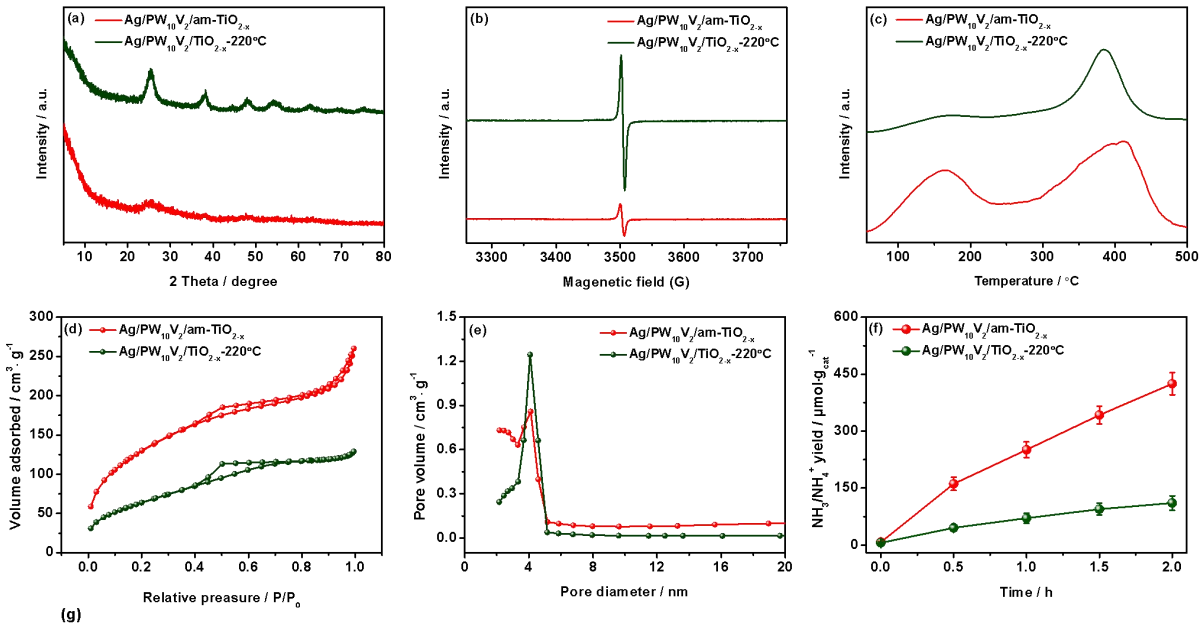

(g)

Catalyst	BET Surface Area ($m^2 \cdot g^{-1}$)	Pore Size (nm)	Pore Volume ($cm^3 \cdot g^{-1}$)	Intensity of EPR	Quantity of chemical adsorption for N_2 ($mmol \cdot g^{-1}$)
$Ag/PW_{10}V_2/TiO_{2-x}$-220°C	237.10	3.2	0.19	5.5	47.5
$Ag/PW_{10}V_2/am\text{-}TiO_{2-x}$	476.57	3.0	0.35	1.3	97.3

Fig. S19. (a) XRD patterns, (b) EPR spectra, (c) N_2-TPD profiles, (d) N_2-absorption-desorption isotherms, (e) BJH pore size distributions, (f) NH_3/NH_4^+ productions for $Ag/PW_{10}V_2/am\text{-}TiO_{2-x}$ and $Ag/PW_{10}V_2/TiO_{2-x}$-220°C, as well as (g) the summary of concerned parameters

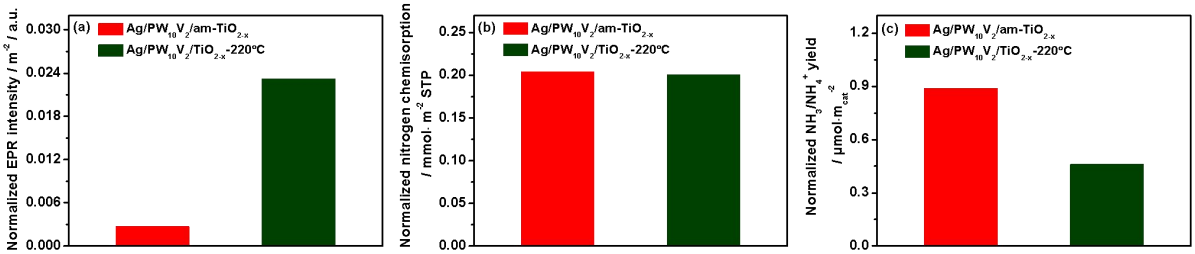

Fig. S20. Normalized (a) EPR intensity, (b) N_2 chemisorption amount and (c) NH_3/NH_4^+ productions for $Ag/PW_{10}V_2/am\text{-}TiO_{2-x}$ and $Ag/PW_{10}V_2/TiO_{2-x}$-220°C

$PW_{10}V_2$ and Ag NPs co-doped TiO_{2-x} ($Ag/PW_{10}V_2/TiO_{2-x}$-220°C) is obtained at solvothermal synthesis of 220°C. As shown in Fig. S19, TiO_{2-x} matrix with anatase crystalline is achieved, together with

intensified EPR signal. This is in line with TiO_{2-x}-220°C as mentioned above.[23] As expected, nitrogen chemisorption amount decreased, as well BET surface area. Then, 111.2 μmol g_{cat}^{-1} of NH_3/NH_4^+ is generated over $Ag/PW_{10}V_2/TiO_{2-x}$-220°C, which is approximately a quarter of that over $Ag/PW_{10}V_2$/am-TiO_{2-x} (424.9 μmol g_{cat}^{-1}). In Fig. S20, both $Ag/PW_{10}V_2/TiO_{2-x}$-220°C and $Ag/PW_{10}V_2$/am-TiO_{2-x} possess similar normalized nitrogen chemisorption amount. However, the normalized NH_3/NH_4^+ production over $Ag/PW_{10}V_2/TiO_{2-x}$-220°C is half of that over $Ag/PW_{10}V_2$/am-TiO_{2-x}. The control experiments evidently highlight amorphous nature of TiO_{2-x} matrix in $Ag/PW_{10}V_2$/am-TiO_{2-x} during photo-driven nitrogen reduction process.

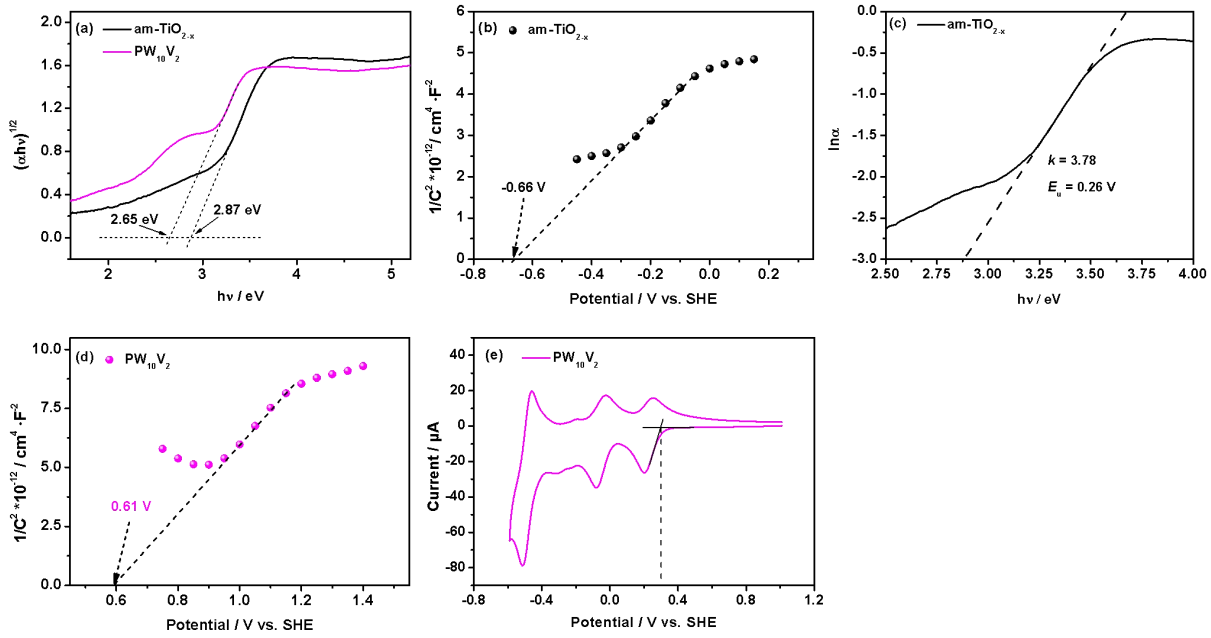

Fig. S21. (a) Tauc plots of am-TiO_{2-x} and $PW_{10}V_2$, (b, d) Mott-Schottky plots of am-TiO_{2-x} and $PW_{10}V_2$, (c) Urbach plot of am-TiO_{2-x}, as well as (e) cyclic voltammogram of $PW_{10}V_2$.

As displayed in Fig. S21a, the values of band gap energy (E_g) of semiconductors are estimated by the x-axis intercepts of Tauc plots as converted from UV-vis diffuse reflectance spectra. The band gap energy of semiconductor am-TiO_{2-x} is determined to be 2.87 eV, as well 2.65 eV for semiconductor-like $PW_{10}V_2$. Both of them are classified to be *n*-type semiconductors according to their positive slopes in Mott-Schottky plots, and their flat band potentials are estimated to be -0.66 and 0.61 V for am-TiO_{2-x} and $PW_{10}V_2$, respectively. For am-TiO_{2-x}, the defect state induced by OVs below CB can be determined by the Urbach plot according to the formula $\alpha = \alpha_0 exp(h\nu/E_u)$.[24] Here, α is the absorption coefficient, α_0 is a constant, $h\nu$ is the incident photon energy and E_u is the Urbach energy (*i.e.* energy level difference from the defect state to CBM). Then, lnα is plotted against $h\nu$ (Fig. S21c), and E_u is the reciprocal of the slope. Accordingly, E_u is estimated to be 0.26 eV for am-TiO_{2-x}, namely, defect state is 0.26 eV below CBM. With respect to $PW_{10}V_2$, its LUMO level (0.30 V *vs* SHE) is estimated by onset potential for the first reduction peak in cyclic voltammogram.[25]

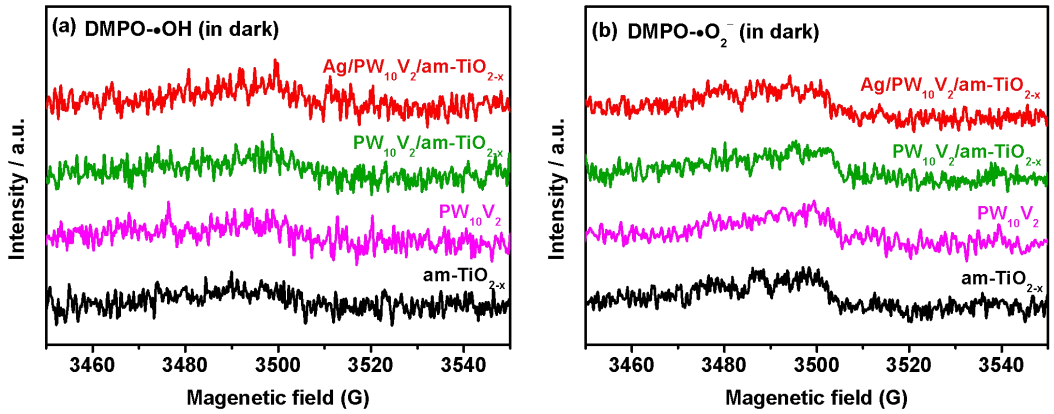

Fig. S22. DMPO spin-trapping EPR spectra in (a) aqueous dispersion and (b) methanol dispersion without irritation

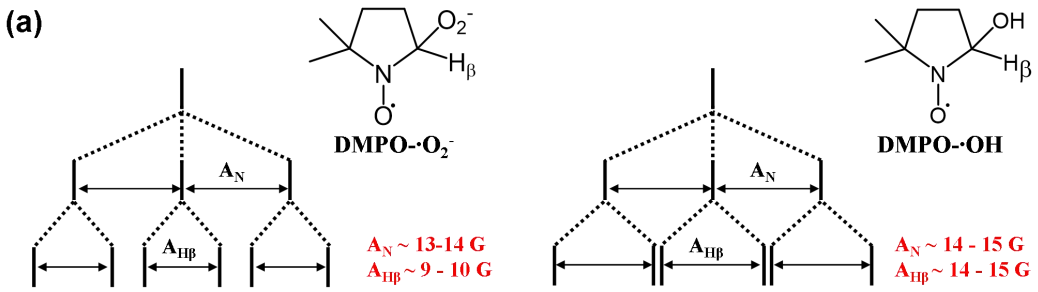

(b)

Catalysts	Redical	g-factor	A_N (G)	$A_{H\beta}$ (G)
am-TiO_{2-x}	DMPO-·OH	—	—	—
$PW_{10}V_2$	DMPO-·OH	2.006(1)	14.98	14.72
$PW_{10}V_2$/am-TiO_{2-x}	DMPO-·OH	2.006(2)	14.97	14.67
Ag/$PW_{10}V_2$/am-TiO_{2-x}	DMPO-·OH	2.006(2)	14.94	14.69
am-TiO_{2-x}	DMPO-·O_2^-	2.006(5)	13.54	9.69
$PW_{10}V_2$	DMPO-·O_2^-	—	—	—
$PW_{10}V_2$/am-TiO_{2-x}	DMPO-·O_2^-	2.006(5)	13.61	9.62
Ag/$PW_{10}V_2$/am-TiO_{2-x}	DMPO-·O_2^-	2.006(6)	13.54	9.81

Fig. S23. (a) Schematic diagram of the EPR hyperfine splitting for DMPO-·OH and DMPO-·O_2^- adducts, as well as (b) corresponding g-factors, A_N(G) and $A_{H\beta}$(G) values

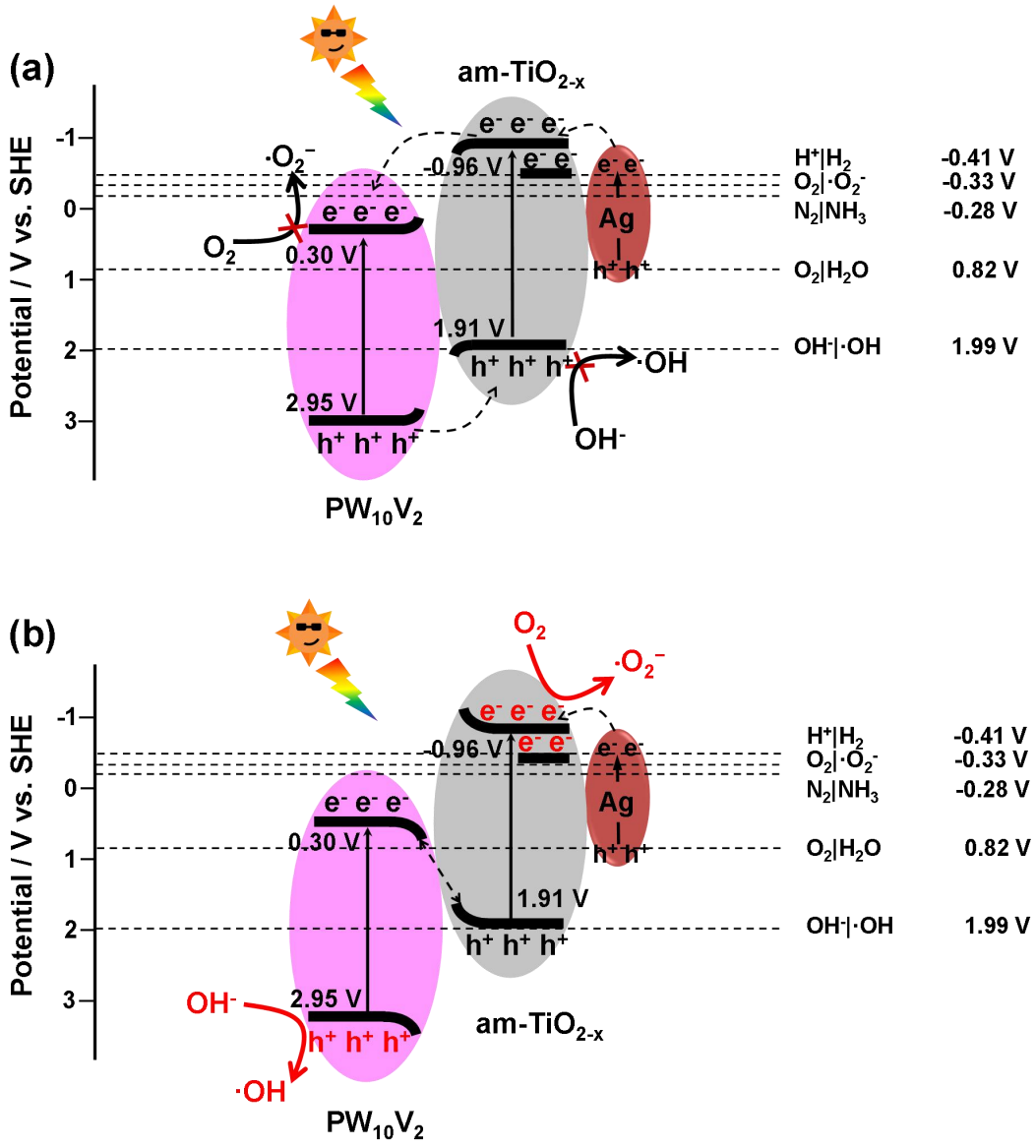

Scheme S1. Two different types of charge carrier separation and migration mechanism of the $Ag/PW_{10}V_2/am\text{-}TiO_{2-x}$ heterojunctions

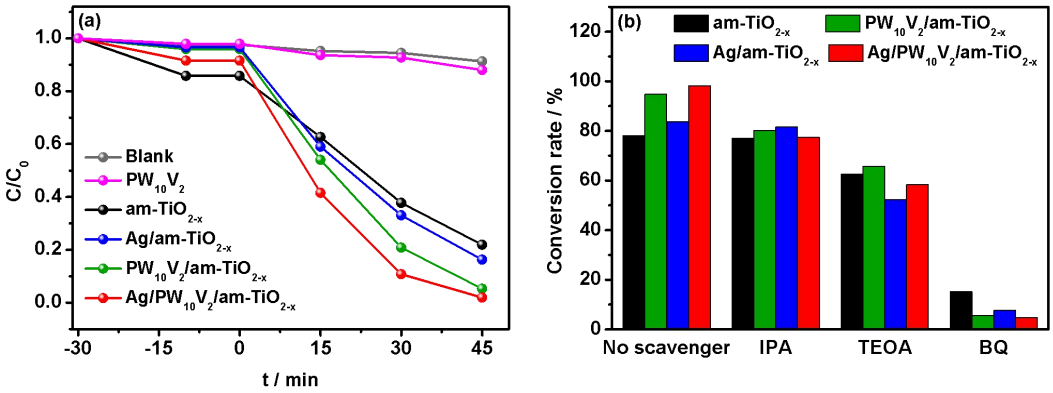

Fig. S24. (a) The photocatalytic activities of as-prepared catalysts for MO degradation under simulated sunlight and (b) corresponding trapping experiments for active species

To further verify the proposed mechanism in the $Ag/PW_{10}V_2/am\text{-}TiO_{2\text{-}x}$ photocatalytic system, the photocatalytic activities of as-prepared catalysts are evaluated in degradation of MO. As shown in Fig. S24a, $PW_{10}V_2/am\text{-}TiO_{2\text{-}x}$ still exhibits remarkably higher activity than those of neat $PW_{10}V_2$ and $am\text{-}TiO_{2\text{-}x}$. Then, trapping experiments for active species are carried out to investigate the enhancing mechanism of photocatalytic system (Fig. S24b), where isopropanol (IPA), triethanolamine (TEOA) and 1,4-benzoquinone (BQ) are used as trapping agent for ·OH, photo-generated holes and $\cdot O_2^-$, respectively. For neat $am\text{-}TiO_{2\text{-}x}$, when introducing IPA into reaction solution, the photocatalytic degradation rate stays invariably, whereas slight decrease is observed when the TEOA is added into reaction solution. In contrast, the degradation is almost inhibited when BQ is introduced into the reaction medium. This means that $\cdot O_2^-$ and holes are the major reactive species in the catalytic system of neat $am\text{-}TiO_{2\text{-}x}$. For $PW_{10}V_2/am\text{-}TiO_{2\text{-}x}$, the photocatalytic degradation rate decreases by ca. 15% and 30% when the IPA and TEOA were added into reaction solution, respectively; whereas it decreases significantly when BQ were added. Similar phenomenon occurs as well in the catalytic system of $Ag/PW_{10}V_2/am\text{-}TiO_{2\text{-}x}$. This phenomenon indicates that ·OH, holes and $\cdot O_2^-$ all participate in the reaction, they are all the major reactive species in the catalytic system of $PW_{10}V_2/am\text{-}TiO_{2\text{-}x}$ and $Ag/PW_{10}V_2/am\text{-}TiO_{2\text{-}x}$. The presence

of $\cdot O_2^-$ in am-TiO_{2-x} system was confirmed by EPR trapping experiments; as well the presence of $\cdot O_2^-$ and ·OH in $PW_{10}V_2$/am-TiO_{2-x} and Ag/$PW_{10}V_2$/am-TiO_{2-x} systems (Fig. 5d and e in main text).

On the basic of the above experimental results, a photocatalytic mechanism for the enhanced activity of Ag/$PW_{10}V_2$/am-TiO_{2-x} heterojunction was proposed (Scheme S1b). If the heterojunction between $PW_{10}V_2$ and am-TiO_{2-x} fits type-II mechanism (Scheme S1a), $\cdot O_2^-$ cannot be generated from the accumulated photogenerated electrons on the LUMO orbital of $PW_{10}V_2$, and ·OH cannot be generated on the VB of am-TiO_{2-x}. Thus, Z-scheme mechanism is suggested (Scheme S1b). In this way, the more photogenerated holes accumulated at HOMO of $PW_{10}V_2$ can oxidize OH^- to form more ·OH, the more photogenerated electrons accumulated in the CB of am-TiO_{2-x} can reduce the adsorbed O_2 to form more $\cdot O_2^-$, which are powerful species that can break down the chromophores of organic pollutants into small molecules. Meanwhile, the photogenerated holes left behind in the HOMO of $PW_{10}V_2$ can directly oxidize organic pollutants.

Table S4. Decay time of am-TiO_{2-x}, $PW_{10}V_2$, $PW_{10}V_2$/am-TiO_{2-x}, Ag/am-TiO_{2-x} and Ag/$PW_{10}V_2$/am-TiO_{2-x} derived from time-resolved PL curves

Samples	τ_1 (ns) /Int. (%)	τ_2 (ns) /Int. (%)	τ_{av}(ns)
$PW_{10}V_2$	1.14/60.94	6.73/39.06	5.56
am-TiO_{2-x}	1.08/59.47	5.81/40.53	4.79
Ag/am-TiO_{2-x}	1.27/50.31	9.81/49.69	8.82
$PW_{10}V_2$/am-TiO_{2-x}	0.97/50.30	7.60/49.70	6.84
$PW_{10}V_2$/Ag/am-TiO_{2-x}	1.22/50.88	14.22/49.12	13.15

Note: A two-exponential function equation is used to fit the decay time. Fast decay component (τ_1 and A_1) and slow component (τ_2 and A_2) are obtained, deriving from the free excited states and the bound excited states, respectively. The average decay time is calculated according to equation $\tau_{av} = (A_1 \cdot \tau_1^2 + A_2 \cdot \tau_2^2)/(A_1 \cdot \tau_1 + A_2 \cdot \tau_2)$, where τ and A are decay time and the relative intensity, respectively.

Table S5. Transient photocurrent intensity of $PW_{10}V_2$, am-TiO_{2-x}, $PW_{10}V_2$/am-TiO_{2-x}, Ag/am-TiO_{2-x} and Ag/$PW_{10}V_2$/am-TiO_{2-x}

Samples	I_1(μA)	I_2(μA)	I_3(μA)	I_4(μA)	I_5(μA)	I_{av}(μA)
$PW_{10}V_2$	0.29	0.29	0.29	0.28	0.28	0.29
am-TiO_{2-x}	0.24	0.25	0.24	0.25	0.24	0.24
$PW_{10}V_2$/am-TiO_{2-x}	0.33	0.34	0.34	0.34	0.33	0.34
Ag/am-TiO_{2-x}	0.41	0.43	0.42	0.42	0.42	0.42
Ag/$PW_{10}V_2$/am-TiO_{2-x}	0.61	0.62	0.62	0.62	0.62	0.62

Table S6. The resistance of am-TiO_{2-x}, $PW_{10}V_2$, $PW_{10}V_2$/am-TiO_{2-x}, Ag/am-TiO_{2-x} and Ag/$PW_{10}V_2$/am-TiO_{2-x} obtained by EIS Nyquist plots

Samples	R_e(Ω)	R_{ct}(Ω)
$PW_{10}V_2$	63.34	28.32
am-TiO_{2-x}	64.92	29.07
$PW_{10}V_2$/am-TiO_{2-x}	74.39	26.21
Ag/am-TiO_{2-x}	50.99	23.89
Ag/$PW_{10}V_2$/am-TiO_{2-x}	60.07	22.44

3. References

1 X. Gao, Y. Wen, D. Qu, L. An, S. Luan, W. Jiang, X. Zong, X. Liu and Z. Sun, *ACS Sustainable Chem. Eng.*, 2018, **6**, 5342-5348.

2 S. Sun, P. Song, J. Cui and S. Liang, *Catal. Sci. Technol.*, 2019, **9**, 4198-4215.

3 S. Tang, W. Wu, Z. Fu, S. Zou, Y. Liu, H. Zhao, S.R. Kirk and D. Yin, *ChemCatChem*, 2015, **7**, 2637-2645.

4 H. Shi, Y. Yu, Y. Zhang, X. Feng, X. Zhao, H. Tan, S.U. Khan, Y. Li and E. Wang, *Appl. Catal., B*, 2018, **221**, 280-289.

5 Y. Zhao, Y. Zhao, G.I.N. Waterhouse, L. Zheng, X. Cao, F. Teng, L.Z. Wu, C.H. Tung, D. O'Hare and T. Zhang, *Adv. Mater.*, 2017, **29**, 1703828.

6 S. Sun, X. Li, W. Wang, L. Zhang and X. Sun, *Appl. Catal., B*, 2017, **200**, 323-329.

7 X. Li, W. Wang, D. Jiang, S. Sun, L. Zhang and X. Sun, *Chem. - Eur. J.*, 2016, **22**, 13819-13822.

8 P. Li, Z. Zhou, Q. Wang, M. Guo, S. Chen, J. Low, R. Long, W. Liu, P. Ding, Y. Wu and Y. Xiong, *J. Am. Chem. Soc.*, 2020, **142**, 12430-12439.

9 S. Wang, X. Hai, X. Ding, K. Chang, Y. Xiang, X. Meng, Z. Yang, H. Chen and J. Ye, *Adv. Mater.*, 2017, **29**, 1701774.

10 Y. Lu, Y. Yang, T. Zhang, Z. Ge, H. Chang, P. Xiao, Y. Xie, L. Hua, Q. Li, H. Li, B. Ma, N. Guan, Y. Ma and Y. Chen, *ACS Nano*, 2016, **10**, 10507-10515.

11 C. Xiao, L. Zhang, K. Wang, H. Wang, Y. Zhou and W. Wang, *Appl. Catal., B*, 2018, **239**, 260-267.

12 N. Zhang, A. Jalil, D. Wu, S. Chen, Y. Liu, C. Gao, W. Ye, Z. Qi, H. Ju, C. Wang, X. Wu, L. Song, J. Zhu and Y. Xiong, *J. Am. Chem. Soc.*, 2018, **140**, 9434-9443.

13 X. Xue, R. Chen, C. Yan, Y. Hu, W. Zhang, S. Yang, L. Ma, G. Zhu and Z. Jin, *Nanoscale*, 2019, **11**, 10439-10445.

14 J. Liu, R. Li, X. Zu, X. Zhang, Y. Wang, Y. Wang and C. Fan, *Chem. Eng. J.*, 2019, **371**, 796-803.

15 X. Gao, Y. Shang, L. Liu and F. Fu, *J. Catal.*, 2019, **371**, 71-80.

16 S. Wu, X. Tan, K. Liu, J. Lei, L. Wang and J. Zhang, *Catal. Today*, 2019, **335**, 214-220.

17 Y. Li, X. Chen, M. Zhang, Y. Zhu, W. Ren, Z. Mei, M. Gu and F. Pan, *Catal. Sci. Technol.*, 2019, **9**, 803-810.

18 Y. Hao, X. Dong, S. Zhai, H. Ma, X. Wang and X. Zhang, *Chem. - Eur. J.*, 2016, **22**, 18722-18728.

19 H. Li, J. Shang, Z. Ai and L. Zhang, *J. Am. Chem. Soc.*, 2015, **137**, 6393-6399.

20 L. Ye, C. Han, Z. Ma, Y. Leng, J. Li, X. Ji, D. Bi, H. Xie and Z. Huang, *Chem. Eng. J.*, 2017, **307**, 311-318.

21 X. Gao, Y. Shang, L. Liu and F. Fu, *J. Colloid Interface Sci.*, 2019, **533**, 649-657.

22 A.M. Khenkin, P. Carl, D. Baute, A.M. Raitsimring, A.V. Astashkin, L.J.W. Shimon, D. Goldfarb and R. Neumann, *Inorg. Chim. Acta*, 2006, **359**, 3072-3078.

23 L. Xu, X. Ma, N. Sun and F. Chen, *Appl. Surf. Sci.*, 2018, **441**, 150-155.

24 X.Y. Kong, W.Q. Lee, A.R. Mohamed and S.-P. Chai, *Chem. Eng. J.*, 2019, **372**, 1183-1193.

25 J. Meng, X. Wang, X. Yang, A. Hu, Y. Guo and Y. Yang, *Appl. Catal., B*, 2019, **251**, 168-180.